

PCCP

Physical Chemistry Chemical Physics

Accepted Manuscript

This article can be cited before page numbers have been issued, to do this please use: J. Kumar and G. Sai Gautam, *Phys. Chem. Chem. Phys.*, 2023, DOI: 10.1039/D2CP04453F.



This is an Accepted Manuscript, which has been through the Royal Society of Chemistry peer review process and has been accepted for publication.

Accepted Manuscripts are published online shortly after acceptance, before technical editing, formatting and proof reading. Using this free service, authors can make their results available to the community, in citable form, before we publish the edited article. We will replace this Accepted Manuscript with the edited and formatted Advance Article as soon as it is available.

You can find more information about Accepted Manuscripts in the [Information for Authors](#).

Please note that technical editing may introduce minor changes to the text and/or graphics, which may alter content. The journal's standard [Terms & Conditions](#) and the [Ethical guidelines](#) still apply. In no event shall the Royal Society of Chemistry be held responsible for any errors or omissions in this Accepted Manuscript or any consequences arising from the use of any information it contains.

Study of pnictides for photovoltaic applications

View Article Online
DOI: 10.1039/D2CP04453F

Jayant Kumar¹ and Gopalakrishnan Sai Gautam^{2,*}

Department of Materials Engineering, Indian Institute of Science, Bengaluru 560012, India

*E-mail: saigautamg@iisc.ac.in

¹ORCID: 0000-0001-6454-9623, ²ORCID: 0000-0002-1303-0976

Abstract

For the transition into a sustainable mode of energy usage, it is important to develop photovoltaic materials that exhibit better solar-to-electricity conversion efficiencies, a direct optimal band gap, and made of non-toxic, earth abundant elements compared to the state-of-the-art silicon photovoltaics. Here, we explore the non-redox-active pnictide chemical space, including binary A_3B_2 , ternary AA'_2B_2 , and quaternary $AA'A''B_2$ compounds ($A, A', A'' = \text{Ca, Sr, or Zn}$; $B = \text{N or P}$), as candidate beyond-Si photovoltaics using density functional theory calculations. Specifically, we evaluate the ground state configurations, band gaps, and 0 K thermodynamic stability for all 20 pnictide compositions considered, besides computing the formation energy of cation vacancies, anion vacancies, and cation anti-sites in a subset of candidate compounds. Importantly, we identify SrZn_2N_2 , SrZn_2P_2 , and CaZn_2P_2 to be promising candidates, exhibiting optimal (1.1-1.5 eV) hybrid-functional-calculated band gaps, stability at 0 K, and high resistance to point defects (formation energies >1 eV), while other possible candidates include ZnCa_2N_2 and ZnSr_2N_2 , which may be susceptible to N-vacancy formation. We hope that our study will contribute to the practical development of pnictide semiconductors as beyond-silicon light absorbers.

1 Introduction

View Article Online
DOI: 10.1039/D2CP04453F

The 21st century world is in need of a dramatic shift in the energy sector, given the increasingly unsustainable nature of fossil fuel usage and the associated climate change. Among renewable sources, solar energy, i.e., the conversion of solar radiation into electricity via photovoltaics (PVs), has significant potential in reducing our fossil fuel usage.(1) Notably, the Shockley-Queisser limit for maximum efficiency in single-junction PV devices requires semiconductors with a direct band gap in the 1.1-1.5 eV range.(2) Commercially, PVs are typically made based on crystalline Si, and do require larger material quantities (i.e., PV panels are thick) and higher manufacturing costs, necessitated by the indirect band gap (1.12 eV) of Si.(3) Thus, engineering and discovering direct gap semiconductors, which exhibit a 1.1-1.5 eV band gap, are made out of environmentally sustainable and non-toxic elements, and are reasonably cheap to manufacture, is still an active area of research.(4)·(5)·(6)

Semiconductors that have been explored as potential beyond-Si photovoltaics, which are often compounds, include (In,Ga)As, CdTe, Cu₂ZnSnS₄ (CZTS), Cu₂InGaSe₄ (CIGS), and their doped counterparts. There are several challenges in utilizing the aforementioned compounds as PVs, including some of the elements being toxic (e.g., As in (In,Ga)As), lack of abundance of elements (e.g., Te in CdTe(7)), difficulties in synthesis of phase-pure compounds resulting in the presence of secondary phases (e.g., secondary phases of Cu-Se and Ag-Cu-Se forms in (Ag,Cu)₂(In,Ga)Se₂ (8)) and the spontaneous formation of detrimental point defects (e.g., Cu_{Zn} + Zn_{Cu} and Sn_{Zn} + 2Cu_{Zn} anti-site clusters in CZTS). In particular, point defects that form either during synthesis or processing (e.g., high temperature annealing) can be harmful in reducing PV performance, by introducing structural distortions, altering the band gap, and/or formation of deep trap states within the band gap. Hence, it is important to evaluate the tendency to form intrinsic point defects while considering any novel semiconductor compound as a PV candidate.

Here, we explore a set of 20 pnictide compounds, including binary, ternary, and quaternary nitrides and phosphides, as potential PV candidates, using density functional theory (DFT(9,10)) calculations. Specifically, we explore pnictides of the formula, A₃B₂, AA'B₂, and AA'A''B₂ where A, A' and A'' are permutations of different divalent cations and B is either N³⁻ or P³⁻. We chose the chemical space of the above mentioned pnictides, partly inspired by the works of Kikuchi et al.(11) and Hinuma et al.,(12) with the constraint of choosing elements that are reasonably abundant and non-toxic to humans. Given the general chemical formula of

A_3B_2 , charge neutrality constraints and computational costs, we considered the combinations of several divalent cations in our compositions. Possible divalent cations that can constitute an A_3B_2 pnictide include alkaline earths (Mg, Ca, Sr, and Ba), and transition metals (V, Nb, Mn, Fe, Co, Ni, and Zn). We did not consider transition metals, except Zn, since they are redox-active and can result in acting as recombination centers or carrier traps. We found Mg- and Ba-based nitrides to exhibit band gaps that are higher than the optimal range for photovoltaic applications. For example, $CaMg_2N_2$ exhibits 3.3 eV,⁽¹¹⁾ and $Ca(Mg_{1-x}Zn_x)_2N_2$ can have a band gap in the range of ~3.3-1.9 eV depending on x ,⁽¹³⁾ while $BaMg_2N_2$ and $BaMg_2P_2$ have gaps of 2.49 eV and 1.80 eV, respectively.⁽¹⁴⁾ Thus, we end up with pnictides, where possible cations are Ca, Sr, and Zn. Importantly, our choice of the pnictide chemical space has been explored by a few existing studies as possible PVs, such as Ca_3N_2 , Zn_3N_2 , Zn_3P_2 , and $CaZn_2N_2$,⁽¹⁵⁾⁽¹⁶⁾⁽¹⁷⁾^(12,18) while a widespread theoretical or experimental screening for PV candidates has not been done so far.⁽¹⁹⁾ We do note that our sampling of pnictides is only a subset of the possible compounds that can exist in nature.⁽²⁰⁾

Apart from determining the ground state atomic configuration in disordered compounds, we evaluate their suitability as a PV material by calculating their band gap, 0 K thermodynamic and dynamic stability, and the formation energies of select point defects. Importantly, we identify five potential candidates, namely, $ZnCa_2N_2$, $SrZn_2N_2$, $ZnSr_2N_2$, $CaZn_2P_2$, and $SrZn_2P_2$, which exhibit an optimal (1.1-1.5 eV) band gap and are thermodynamically stable. Among the candidates that we have identified, $CaZn_2N_2$ and $SrZn_2N_2$ have been experimentally reported to exhibit band gaps of 1.90 eV and 1.60 eV, respectively.^(11,12) Notably, considering point defect formation energies, we find $SrZn_2N_2$, $CaZn_2P_2$, and $SrZn_2P_2$ to be particularly promising since they exhibit a formation energy of >1 eV for cation vacancies, anion vacancies, and cation anti-sites. We hope that our study will reinvigorate research in the pnictide chemical space for potential PV materials, and will aid in the development of high efficiency, beyond-Si PVs that consist of sustainable and non-toxic constituents.

2 Methods

We calculated the total energies and electronic structures, for all pnictides considered, using DFT as implemented in the Vienna ab initio simulation package^(21,22) and employing the projector-augmented-wave theory⁽²³⁾ (list of potentials used is provided in the Supporting

Information—SI). We used an energy cut-off of 520 eV on a plane-wave basis for all calculations, after validating the convergence of DFT-calculated total energy with various cut-off energies as shown in **Figure S1** of SI. We sampled the irreducible Brillouin zone using Γ -centred Monkhorst-Pack(24) meshes with a density of 32 k -points per Å, and used a Gaussian smearing with a width of 0.05 eV. We relaxed all structures by allowing the cell shape, cell volume, and ionic positions to change, without preserving symmetry, until the atomic forces and total energies reduced below $|0.01|$ eV/Å, and 10^{-5} eV, respectively, with the stress below a threshold of 0.2 GPa. Although we did not impose any symmetry constraints during our structural relaxation, particularly for the theoretically derived structures, we find the likelihood of the structural relaxation resulting in a structure that has a completely different symmetry from the initial configuration to be highly unlikely, since the theoretical structures were generated by chemical substitution at the uniquely defined symmetric sites.

We treated the electronic exchange-correlation interactions with the strongly constrained and appropriately normed (SCAN(25)) functional for all structure relaxation calculations. For the electronic density of states (DOS) calculations, we considered the converged ground state structure for each composition, and used the “fake” self-consistent field (SCF) procedure, with a mesh density of 64 k -points per Å. Note that the set of k -points sampled during the structure relaxation were retained with their original weights, while the newly introduced k -points were sampled with zero weights within the fake-SCF procedure. Since SCAN typically underestimates the band gap of semiconducting systems,(3),(26),(27),(28),(29),(30) we also performed DOS calculations using the Heyd-Scuseria-Ernzerhof (HSE06(31)) hybrid functional, using an identical fake-SCF procedure and the SCAN-relaxed structures. For a select set of candidate pnictides, we calculated band structures using SCAN and the Setyawan-Curtarolo scheme to generate the list of symmetrically important k -points, as implemented in pymatgen.(32)-(33)

The initial crystal structure for a subset of the compounds considered in this work (see **Table 1**), were obtained from the inorganic crystal structure database (ICSD).(34) The calculated structural and band gap information of all compounds considered are also compiled in **Table S1**. For the remaining compounds, we derived the initial configurations based on the available unique structures of other compounds (i.e., unique space groups) via ionic substitution (see **Section 3.1** for details). For structures that exhibited disorder within the cation and/or anion sub-lattices, we enumerated symmetrically distinct configurations using the OrderDisorderedStructureTransformation() class within pymatgen.(33) Note that the electronic

structure, thermodynamic stability, and defect calculations were performed only for the ground state configuration (as evaluated by DFT) for each compound. To evaluate the thermodynamic stability, we calculated the 0 K convex hulls of the quaternary Ca-Sr-Zn-N and Ca-Sr-Zn-P systems, which includes the elements, and all possible binary, ternary, and quaternary ordered structures, as available in the ICSD.

To determine the dynamic stability and thermal properties of a select set of candidate pnictides, we performed phonon DOS calculations using the phonopy package⁽³⁵⁾ and the SCAN functional. We calculated the real-space force constants from 0.01 Å symmetrically distinct displacements of all atoms within each unit cell. For each atomic displacement, we performed a SCF calculation, with a total-energy convergence threshold of 10^{-6} eV that was sampled at the Γ point of the irreducible Brillouin zone. The resultant phonon frequencies and thermal properties were sampled on a $24 \times 24 \times 24$ mesh and the values are included in **Figures S12** and **S13** of the SI, respectively. Note that negative frequencies in **Figure S12** correspond to imaginary phonon modes. The thermal properties in **Figure S13** are calculated ignoring any imaginary phonon modes and are normalized per formula unit for each composition.

For the five candidates, namely ZnCa_2N_2 , ZnSr_2N_2 , SrZn_2N_2 , CaZn_2P_2 , and SrZn_2P_2 , we calculated the defect formation energies of cation vacancies, anion vacancies, and cation anti-sites. We used $3 \times 3 \times 2$ (90-atom) supercells of CaZn_2P_2 , SrZn_2P_2 , and SrZn_2N_2 and $3 \times 3 \times 2$ (180-atom) supercells of ZnCa_2N_2 and ZnSr_2N_2 to model the defective structures. The formation energy of any defect (E^f) is given by:⁽³⁶⁾

$$E^f = E_{\text{defect}} - E_{\text{bulk}} - \sum_i n_i \mu_i + qE_F + E_{\text{corr}}$$

where E_{defect} and E_{bulk} are the total energies of supercell with and without defect, respectively, n_i represents the number of i -species atoms added (> 0) and/or removed (< 0) to form the defect with μ_i the corresponding chemical potential. We obtained the range of relevant μ_i for all vacancy defects considered from our 0 K convex hulls (values listed in **Table S2** of SI; details of estimating μ ranges for each defect also provided in SI). The terms qE_F and E_{corr} indicate the exchange of charge(s) with the Fermi energy (E_F) of the pristine semiconductor and the corresponding correction term, which are relevant for the formation of charged defects. However, we have only considered neutral defects ($q = E_{\text{corr}} = 0$), which corresponds to removing (or adding) the entire atom to form a defect.

View Article Online
DOI: 10.1039/D2CP04453F

3 Results

3.1 Structures

Table 1: Details of structures obtained from ICSD, with their corresponding space groups. O and D indicate ordered and disordered structures, respectively. The number of unique orderings obtained upon enumeration are listed for disordered structures. The Wyckoff positions of unique cation sites are displayed in the final column on the right. The “*” in the space group column indicate the structures that were used as templates for generating other ternary, and quaternary compositions.

Compounds	Space group	Ordered/Disordered (from ICSD)	Cations/ total atoms	Number of unique orderings	Occupancy (cations per site)	Unique cation sites	
Ca ₃ N ₂	Ia $\bar{3}$	O	24/40	1	Ca: 1.0	48e	
Zn ₃ N ₂					Zn: 1.0		
Ca ₃ P ₂	P6 ₃ /mcm	D	9/15	2	Ca: 0.9	4d, 6g	
Sr ₃ P ₂	I $\bar{4}$ 3d		24/40	18	Sr: 1.0	16c	
Zn ₃ P ₂	P4 ₂ /nmc*	O		3/5	1	Zn: 1.0	8g, 8g, 8g
CaZn ₂ P ₂	P $\bar{3}$ m1*		Ca: 1.0, Zn: 1.0			1a, 2d	
SrZn ₂ P ₂			Sr: 1.0, Zn: 1.0				
ZnSr ₂ N ₂	I4/mmm*		6/10			Zn: 1.0, Ca: 1.0	2a, 4e
ZnCa ₂ N ₂						Zn: 1.0, Ca: 1.0	
ZnSr ₂ P ₂	P6 ₃ /mmc	D	3/5		Zn: 0.5, Sr: 1.0	2a, 2d	

Among the 20 pnictides considered in this work, the ICSD contains structures of 10 compounds, with the structural data compiled in **Table 1** and the initial structures displayed in **Figure 1**. The 10 compounds in **Table 1** crystallize in six distinct space groups, namely anti-bixbyite *Ia* $\bar{3}$ (for Ca₃N₂ and Zn₃N₂, **Figure 1a**), cubic *I* $\bar{4}$ 3*d* (Sr₃P₂, **Figure 1c**), tetragonal *P*4₂/*nmc* (Zn₃P₂, **Figure 1e**), tetragonal *I*4/*mmm* (ZnSr₂N₂ and ZnCa₂N₂, **Figure 1f**), hexagonal *P* $\bar{3}$ *m*1 (CaZn₂P₂ and SrZn₂P₂, **Figure 1d**), and hexagonal *P*6₃/*mmc* (Ca₃P₂ of **Figure 1b** and ZnSr₂P₂ of **Figure 1g**).^{(37)(12,38,39)(40–42)} For the disordered space groups in the ICSD, namely *Ia* $\bar{3}$, *P*6₃/*mmc*, and *I* $\bar{4}$ 3*d* (see **Table 1**), we enumerate and obtain the symmetrically distinct orderings, with **Figure 1** displaying the lowest energy initial configurations for each space group. In the case of *I* $\bar{4}$ 3*d*-Sr₃P₂, we used a 3 × 1 × 1 supercell for enumerating the disordered P sites, resulting in a 40-atom cell, while for other structures we used the unit cell for enumeration. For compounds whose structures are not available in the ICSD, we used the ordered structures with unique space groups in **Table 1** (marked by “*” in the “Space group” column) as templates and used chemical substitution and/or enumeration to derive the new initial structures. Details on the specific templating structures used with examples is provided in the SI. The DFT-calculated energies for the different initial configurations and the ground states (initial configurations) for all theory-derived structures are compiled in **Table S3**, **S4**, and **Figure S2** of the SI.

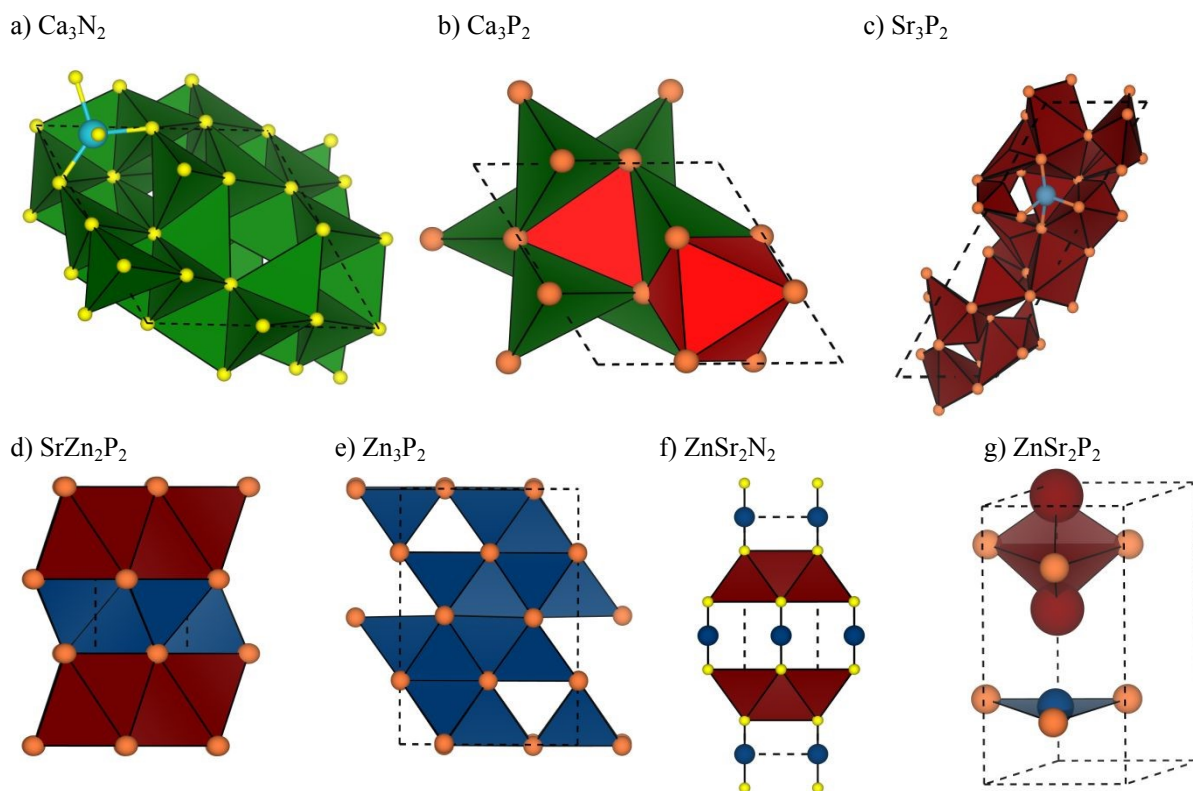


Figure 1: Initial structures of nitrides and phosphides, as available in the ICSD, including a) $Ia\bar{3}$ - Ca_3N_2 (and Zn_3N_2), b) $P6_3/mcm$ - Ca_3P_2 , c) $I\bar{4}3d$ - Sr_3P_2 , d) $P\bar{3}m1$ - SrZn_2P_2 (and CaZn_2P_2), e) $P4_2/nmc$ - Zn_3P_2 , f) $I4/mmm$ - ZnSr_2N_2 (and ZnCa_2N_2), and g) $P6_3/mmc$ - ZnSr_2P_2 . The open polyhedron (panel a) shows the tetrahedral coordination of the Ca (or Sr) atom in Ca_3N_2 (in Sr_3P_2). Different shades of polyhedra in Ca_3P_2 (panel b) show the different coordination environments of tetrahedra (dark green) and octahedra (red) for Ca atom. Panels d, e, and f are used as templates for generating other pnictide compositions. Color codes: Ca – green, Sr – brown, Zn – blue, N – yellow, and P – orange. In panels d and f, Ca and Sr occupy identical sites in the corresponding Sr- and Ca-containing compounds.

3.2 Band gaps

Table 2: Band gaps (E_g in eV) of the pnictides considered in this work, as calculated using the SCAN and HSE06 functionals. Expt. indicates experimental data. The structural origin column indicates whether the initial structure was obtained from ICSD or via theoretical substitution of atoms. Space group of theoretical pnictides are based on the parent templates used.

Compounds	Structural origin	Space group	E_g (eV)		
			SCAN	HSE06	Expt.
Binaries					
Ca_3N_2	ICSD	$Ia\bar{3}$	1.19	1.75	1.90 (15)
Ca_3P_2		$P6_3/mcm$	0.35	0.59	-
Sr_3N_2	Theoretical	$Ia\bar{3}$	0.40	0.93	-
Sr_3P_2	ICSD	$I\bar{4}3d$	0.12	0.38	-
Zn_3N_2		$Ia\bar{3}$	Metallic	0.64	1.23 (43)
Zn_3P_2		$P4_2/nmc$	0.38	0.90	1.46 (17)
Ternaries					
CaSr_2N_2	Theoretical	$P4_2/nmc$	0.71	1.22	-
CaSr_2P_2			1.46	1.75	-
SrZn_2N_2		$P\bar{3}m1$	0.67	1.39	1.60 (11)
SrZn_2P_2	ICSD		0.84	1.18	-
CaZn_2N_2	Theoretical		0.88	1.65	1.90 (12)
CaZn_2P_2	ICSD		0.88	1.23	-
SrCa_2N_2	Theoretical		1.85	2.36	-
SrCa_2P_2			1.73	2.12	-
ZnCa_2N_2	ICSD	$I4/mmm$	0.74	1.40	1.60 (12)
ZnCa_2P_2	Theoretical		0.36	0.80	-
ZnSr_2N_2	ICSD		0.89	1.38	-
ZnSr_2P_2		$P6_3/mmc$	Metallic	0.12	-
Quaternaries					
CaSrZnN_2	Theoretical	$I4/mmm$	0.77	1.33	-
CaSrZnP_2		$P\bar{3}m1$	1.01	1.41	-

All band gap (E_g) data, including the HSE06-calculated, SCAN-calculated, and available experimental values, are compiled in **Table 2**, which also lists whether the calculated DOS is originally from ICSD or a theoretical structure (see **Section 3.1**). In the case of SrZn_2N_2 and CaZn_2N_2 , the E_g has been measured experimentally(11,12), and the structures reported to be trigonal ($P\bar{3}m1$), in accordance with our results. However, the reported structures of SrZn_2N_2 and CaZn_2N_2 are not available in the ICSD, due to which we utilized our template+substitution strategy to obtain initial structures for our calculations. Notably, we find that all our SCAN-calculated E_g (in **Table 2**) are lower than HSE06-calculated E_g , which is expected since the inclusion of exact exchange in hybrid functionals facilitates electron localization and hence result in larger E_g than semi-local functionals (such as SCAN). There are also cases, namely Zn_3N_2 and ZnSr_2P_2 , where SCAN predicts a qualitatively different (i.e., metallic) electronic

structure compared to HSE06, but such compounds may not be candidates for solar absorbers since their actual E_g may be low (i.e., < 1 eV).

Interestingly, there are cases of nitrides exhibiting larger E_g than phosphides of the same cation composition (e.g., Ca_3N_2 vs. Ca_3P_2 , and ZnCa_2N_2 vs. ZnCa_2P_2), while the vice-versa is also true in some cases (e.g., Zn_3P_2 vs. Zn_3N_2 , and CaSr_2P_2 vs. CaSr_2N_2). Importantly, the HSE06- E_g are in better agreement (but underestimating) with respect to the available experimental E_g than SCAN. The level of E_g underestimation by HSE06 is severe in binary pnictides (48% and 38% in Zn_3N_2 and Zn_3P_2 , respectively), compared to the ternaries (13%, 13%, and 12.5% in SrZn_2N_2 , CaZn_2N_2 , and ZnCa_2N_2 , respectively). Thus, for the selection of candidates with suitable band gaps for PV applications, we can still use the general range of 1.1-1.5 eV to ensure that there are no false negatives among the compositions considered.

Applying the 1.1-1.5 eV range within our HSE06- E_g , we find 6 possible ternary pnictides as candidate PVs, namely CaSr_2N_2 ($E_g \sim 1.22$ eV), SrZn_2N_2 (1.39 eV), SrZn_2P_2 (1.18 eV), CaZn_2P_2 (1.23 eV), ZnCa_2N_2 (1.40 eV), and ZnSr_2N_2 (1.38 eV), apart from the quaternaries, CaSrZnN_2 (1.33 eV) and CaSrZnP_2 (1.41 eV). Our calculated band gap in ZnSr_2N_2 (1.38 eV) is in agreement with a previous study utilizing the modified Becke-Johnson potential(44) (~ 1.45 eV(45)), although our predicted value for ZnCa_2N_2 (1.40 eV) is quite different from the same report (~ 1.72 eV(45)). **Figure 2** compiles the HSE06-calculated DOS for the six candidate ternaries, while the remaining HSE06 and SCAN-calculated DOS for all pnictides considered are displayed in the SI (**Figures S3-S9**). The SCAN-calculated band structures for the six candidate pnictides are included in **Figure S10** and an examination of correlation between SCAN-calculated formation energies and band gaps is explored in **Figure S11**. In all our DOS plots, the orange lines correspond to the anion (i.e., N or P) p states, while the red, green, purple, and/or brown lines correspond to the cation s (for Ca, Sr, and Zn) and/or d (for Zn only) states. The dotted blue lines in our DOS panels indicate the valence and conduction band edges, while the Fermi level in metallic systems is displayed by dashed black lines. The zero on the energy scale in all DOS visualizations is set to the valence band maximum (VBM) in gapped systems, while the zero is set to the Fermi level in metallic systems.

Among the candidate ternaries, the VBM consists almost exclusively of the anionic p states, with low overlap of cationic s or d states, suggesting that the cation-anion bonds are quite ionic in nature. While anionic p states dominate the conduction band minimum (CBM)

in CaSr_2N_2 (**Figure 2a**), ZnCa_2N_2 (**Figure 2e**) and ZnSr_2N_2 (**Figure 2f**), the Zn *s* states do contribute significantly to the CBM in SrZn_2N_2 (**Figure 2b**), SrZn_2P_2 (**Figure 2c**), and CaZn_2P_2 (**Figure 2d**). For ternary Zn-containing pnictides, we note that the HSE06-CBM is dominated by anionic *p* in nitrides, while Zn *s* states dominate CBM in phosphides, as illustrated by SrZn_2N_2 (**Figure 2b**)- SrZn_2P_2 (**Figure 2c**), and ZnSr_2N_2 (**Figure 2f**) and ZnSr_2P_2 (**Figure S8d**) pairs. However, for the ZnCa_2N_2 (**Figure 2e**) and ZnCa_2P_2 (**Figure S8c**) pair, the anionic *p* dominates the CBM. Thus, cationic contributions to the CBM in ternaries, if any, only arise in Zn-containing compounds.

In the case of quaternaries, anionic *p* states dominates the VBM in both compounds, while N *p* and Zn *s* states dominate CBM in CaSrZnN_2 (**Figure S7f**) and CaSrZnP_2 (**Figure S9d**) respectively. Among the ternary candidates identified in our work, SrZn_2N_2 , ZnSr_2N_2 , and ZnCa_2N_2 have been explored as solar absorbers before (i.e., E_g calculated and/or measured),^(11,12) while the remaining compounds (CaSr_2N_2 , SrZn_2P_2 , and CaZn_2P_2) have not been studied as PVs so far. However, whether these compounds are feasible PV candidates depends on their thermodynamic stability (**Section 3.3**) and intrinsic tendency to form detrimental point defects (**Section 3.4**). Note that although the experimental band gaps of Zn_3N_2 and Zn_3P_2 are in the optimal range (1.23 eV and 1.46 eV, respectively), previous attempts at utilizing Zn_3P_2 as solar absorbers have yielded poor efficiencies, namely ~4% with expected Mg-doped improvements reaching 8-10% in Zn_3P_2 .⁽⁴⁶⁾ Low efficiency in Zn_3P_2 have been attributed to difficulties in synthesizing *p-n* homojunctions of Zn_3P_2 ,⁽⁴⁶⁾ while the high moisture sensitivity and possible oxygen contamination of Zn_3N_2 has led to large variations in measured band gaps (1.06-3.2 eV),⁽⁴⁷⁾ with possible improvements in band gap engineering arising out of synthesizing $\text{Zn}_{3-3x}\text{Mg}_{3x}\text{N}_2$ alloys.⁽⁴⁸⁾ Hence, we will not be considering Zn_3N_2 and Zn_3P_2 as candidate materials in the rest of the manuscript.

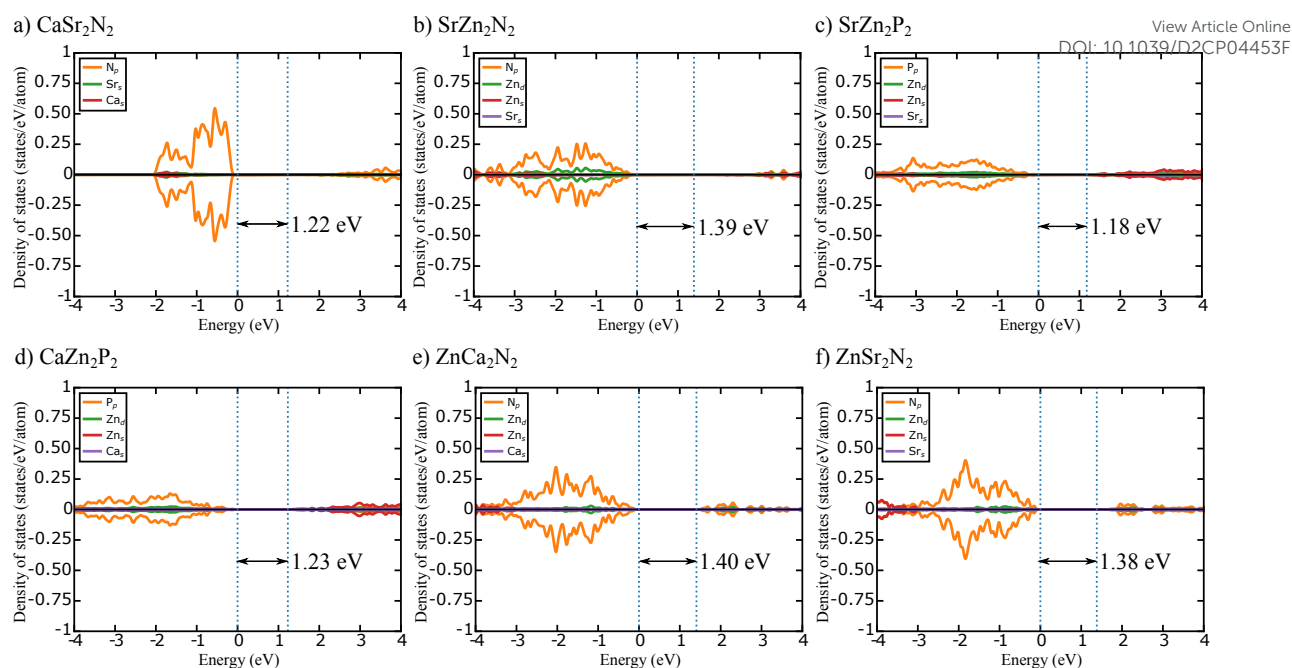


Figure 2: HSE06-calculated DOS for the candidate pnictides. The density of states in each panel is normalized with respect to the total number of atoms within the calculated cell. Text annotation in each panel indicates the calculated band gap with the dotted blue lines highlighting the band edges.

3.3 Thermodynamic stability

We calculated the 0 K convex hulls for the quaternary systems, namely Ca-Sr-Zn-N and Ca-Sr-Zn-P, comprising of all the ordered structures available on ICSD and the theoretical/enumerated ground states that we have considered. For ease of visualization, we have compiled three ternary projections for each quaternary system, namely, Ca-Sr-N, Ca-Zn-N, and Sr-Zn-N (panels **a-c**) for Ca-Sr-Zn-N quaternary, and Ca-Sr-P, Ca-Zn-P, and Sr-Zn-P (panels **d-f**) for Ca-Sr-Zn-P quaternary, in **Figure 3**. All compounds that are stable at 0 K are indicated by green symbols in **Figure 3**. Squares and circles in **Figure 3** indicate the non-candidate and the 20 candidate pnictides considered in this work. Note that previous theoretical studies have utilized a ~ 30 meV/atom energy above the hull (E^{hull}) threshold value,⁽⁴⁹⁾ beyond which synthesis of metastable/unstable compounds may become difficult experimentally. While we use 30 meV/atom as a stability threshold, we note that stability thresholds are often chemistry-dependent and a clear guideline for a threshold is not yet available for pnictides, given that several new compounds are being actively synthesized in this chemical space.⁽²⁰⁾

We find all the ICSD-derived structures to be stable at 0 K, which is in line with expectations that the ICSD-derived structures have been experimentally characterized, with the

only exception being ZnSr_2P_2 that is ~ 90 meV/atom unstable compared to other phases (Sr_3P_2 and SrZn_2P_2) in the Zn-Sr-P phase diagram (**Figure 3f**). Note that the experimental structure of ZnSr_2P_2 is disordered, which typically results in an excess of configurational entropy that may stabilize the compound at higher temperatures, thus facilitating its synthesis. Among the theoretical structures, the stable pnictides are SrZn_2N_2 , CaZn_2N_2 , and SrCa_2P_2 , out of which SrZn_2N_2 and CaZn_2N_2 have been reported to be synthesized before.^(11,12) Thus, we find SrCa_2P_2 to be a stable compound that has not been experimentally reported nor theoretically studied in detail so far.

The unstable ternaries among the pnictides considered are, CaSr_2N_2 ($E^{\text{hull}} \sim 72$ meV/atom), CaSr_2P_2 (65 meV/atom), SrCa_2N_2 (34 meV/atom), and ZnCa_2P_2 (45 meV/atom) with the theoretical binary, Sr_3N_2 also marginally unstable ($E^{\text{hull}} \sim 9$ meV/atom). Both the theoretical quaternaries included in this work, CaSrZnN_2 and CaSrZnP_2 are also unstable ($E^{\text{hull}} \sim 34$ meV/atom and 68 meV/atom, respectively). Given the band gap data of **Table 1** and **Figure 2**, and including the 0 K thermodynamic stability as an additional filter, the set of viable PV candidates reduces to 5 compounds, SrZn_2N_2 , SrZn_2P_2 , CaZn_2P_2 , ZnCa_2N_2 , and ZnSr_2N_2 , thus eliminating CaSr_2N_2 as a candidate due to its thermodynamic instability. Note that although metastable compounds (e.g., CaSrZnN_2) may be synthesizable, such compounds usually exhibit a higher tendency to form point defects than thermodynamically stable compounds.⁽⁵⁰⁾ Hence, for the calculation of point defect energies, we restrict ourselves to the above five candidates.

Notably, we have also evaluated the dynamic stability of the five candidates, by calculating the phonon DOS and the corresponding thermal properties, which are compiled in **Figures S12** and **S13**, respectively. With the exception of ZnSr_2N_2 , we do not find any significant imaginary vibrational modes among the five identified candidates, with numerical noise contributing to minor non-zero imaginary modes (panels a-d in **Figure S12**). In the case of ZnSr_2N_2 , the imaginary mode may have been caused by the unit cell used in the phonon calculation, i.e., we did not evaluate the phonon spectra within a supercell. Given that ZnSr_2N_2 is stable from our 0 K convex hull calculations (**Figure 3c**) and is known to be experimentally synthesizable within the $I4/mmm$ space group,⁽³⁹⁾ we do include ZnSr_2N_2 in the calculations of point defect energetics.

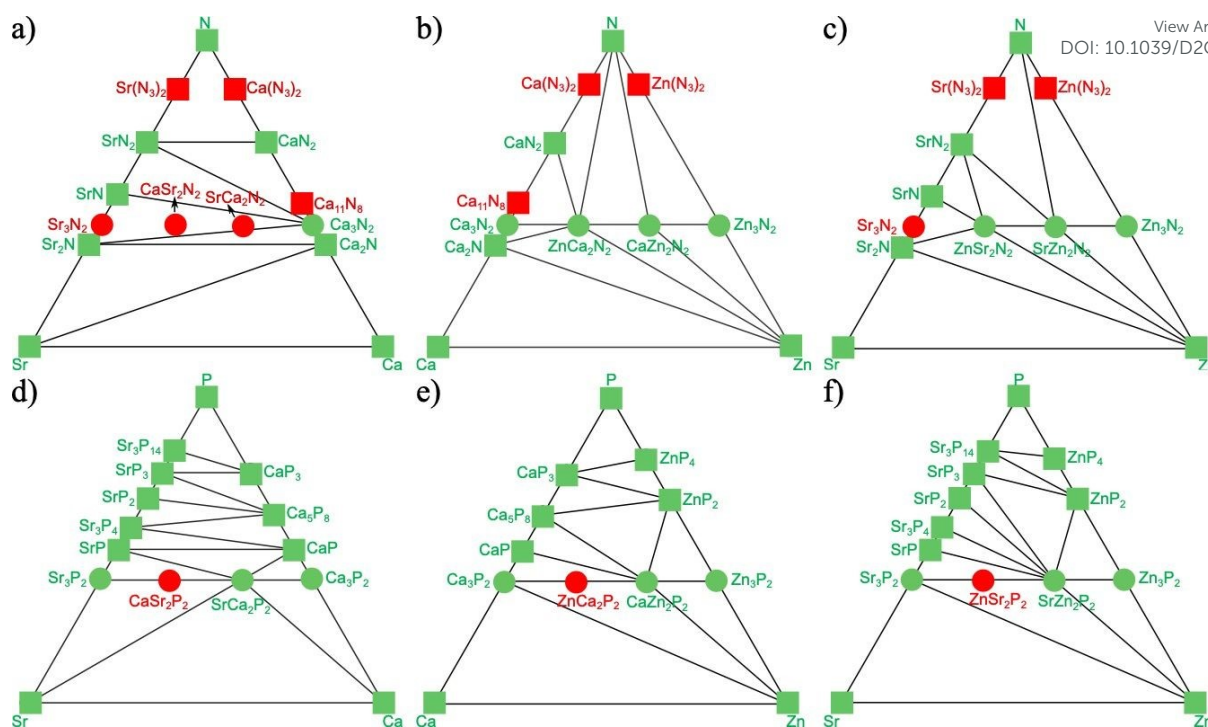


Figure 3: SCAN-calculated 0 K ternary phase diagrams, including (a) Ca-Sr-N, (b) Ca-Zn-N, (c) Sr-Zn-N, (d) Ca-Sr-P, (e) Ca-Zn-P, and (f) Sr-Zn-P systems. Circles and squares correspond to candidate and non-candidate pnictides. Green and red symbols (and corresponding text annotations) are stable and unstable/metastable compounds, respectively.

3.4 Point defect formation energies

For the five candidates identified from our band gap and stability calculations, namely, SrZn_2N_2 , SrZn_2P_2 , CaZn_2P_2 , ZnCa_2N_2 , and ZnSr_2N_2 , we evaluate the point defect energetics, as displayed in **Figure 4**. Specifically, we consider the formation of A and A' cation vacancies (i.e., Vac_A and $\text{Vac}_{A'}$ where Vac is vacancy, yellow and green bars in **Figure 4**), anion vacancies (Vac_B , orange bar), and cation anti-site clusters ($A_A + A'_A$, blue bar). For example, in the case of SrZn_2N_2 , we calculate the energy of formation for Vac_{Sr} , Vac_{Zn} , Vac_{N} , and $\text{Sr}_{\text{Zn}} + \text{Zn}_{\text{Sr}}$ (i.e., Sr occupying a Zn site + Zn occupying a Sr site). Hashed regions in **Figure 4** indicate the variation in the cation/anion vacancy formation energies with the corresponding change in the μ of the species being removed. The range of μ considered is based on the 0 K phase diagrams, i.e., within the region of thermodynamic stability of the pnictide considered. In the case of anti-sites, we created a cluster by exchanging nearest possible neighbors of A and A' atoms. The dashed black line in **Figure 4** indicates a 1 eV threshold of point defect formation energies. Although it is preferable for point defect formation energies to be as high as possible in pristine bulk phases, we use 1 eV as an arbitrary threshold to account for high-temperature synthesis protocols that may be used during fabrication. Additionally, point defects

that exhibit formation energies that are above 1 eV have caused minimal performance deterioration in other candidate photovoltaics, such as kesterite-based chalcogenides.(3,50,51) Note that this 1 eV threshold can be changed, if necessary.

Importantly, we find that all the five candidates exhibit anti-site cluster and cation vacancy formation energies well above the 1 eV threshold (**Figure 4**), ranging from ~ 1.42 eV for Vac_{Ca} in CaZn_2P_2 to 5.25 eV for Vac_{Ca} in ZnCa_2N_2 , highlighting the large degree of resistance that the candidate pnictides exhibit for formation of such defects. In terms of anion vacancies, while SrZn_2N_2 (2.29 – 2.64 eV), SrZn_2P_2 (2.02 – 3.26 eV), and CaZn_2P_2 (1.88 – 3.17 eV) exhibit formation energies above the 1 eV threshold, ZnCa_2N_2 (0.42 – 2.14 eV) and ZnSr_2N_2 (0.47 – 2.00 eV) do not, indicating that the former three compounds exhibit better resistance to *n*-type anion vacancies, especially under anion-poor conditions. Thus, combining the band gap, thermodynamic stability, and high degree of resistance to point defect energetics, we find SrZn_2N_2 , SrZn_2P_2 , and CaZn_2P_2 to be the most promising candidate materials for PV applications. In case low temperature synthesis and/or heat treatment protocols are utilized, we believe that ZnCa_2N_2 and ZnSr_2N_2 may also be relevant for PVs, since their defect formation energies are higher than the values reported for common point defects in kesterite-based PV materials.(3,29,52,53) While SrZn_2N_2 has been explored for its semiconducting properties before(11), SrZn_2P_2 and CaZn_2P_2 are novel candidates whose electronic properties have not been explored *a priori*.

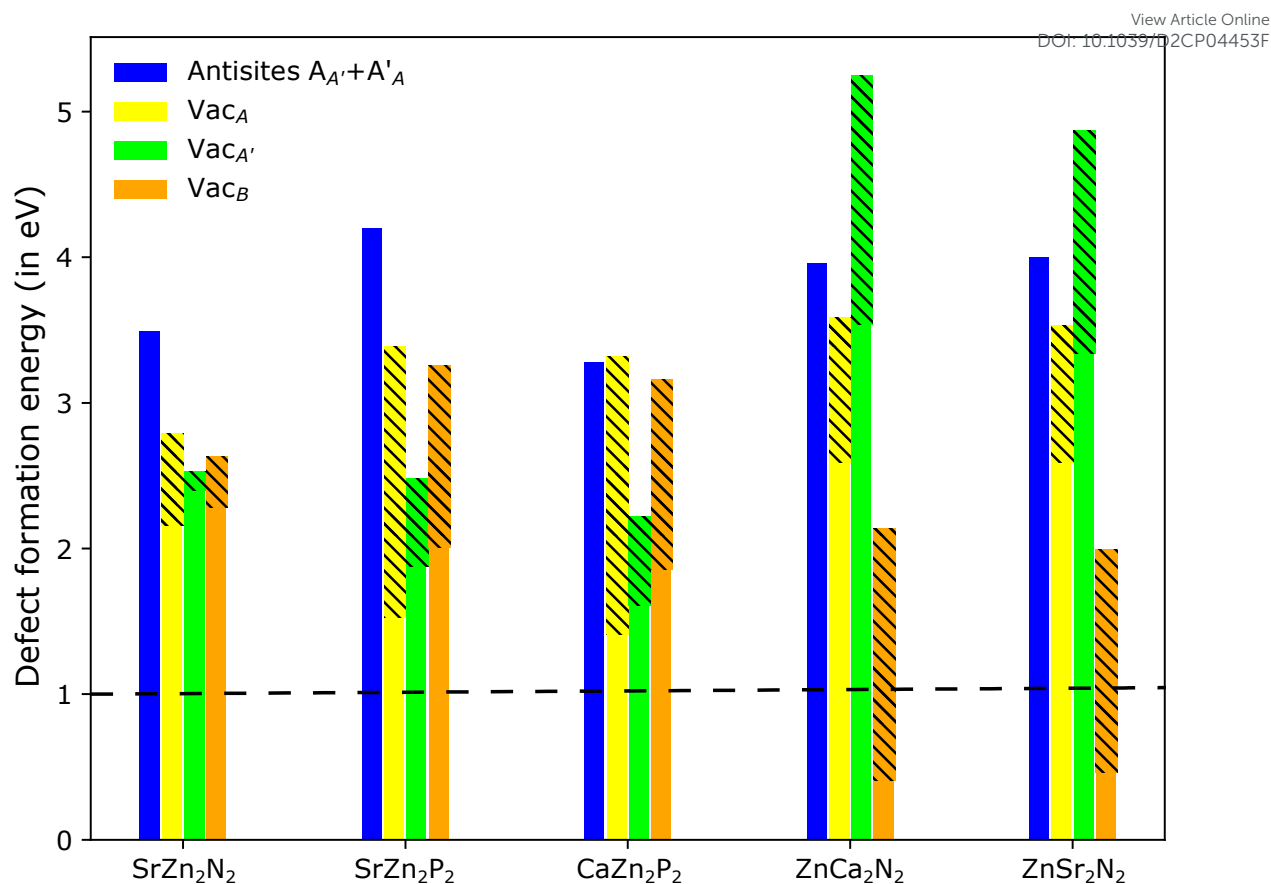


Figure 4: Point defect formation energies for A-site and A'-site cation vacancies (Vac_A and Vac_{A'}, yellow and green bars), anion vacancies (Vac_B), and cation anti-site clusters (A_{A'}+A'_A). The ternaries considered exhibit a composition of AA'₂B₂. Hashed regions signify variation in vacancy formation energies with change in the chemical potential of the species removed.

4 Discussion

Using DFT calculations, we have explored the binary, ternary, and quaternary divalent-metal-based pnictide chemical space as candidate beyond-Si photovoltaic materials in this work. Specifically, we considered a set of twenty compounds, comprising A₃B₂ binaries, AA'₂B₂ ternaries, and AA'A''B₂ quaternaries (A, A', A'' = Ca, Sr, or Zn; B = N or P) and quantified their ground state configurations, band gaps, 0 K thermodynamic stability, dynamic stability via phonon calculations, and formation energies of select point defects. Importantly, we identified SrZn₂N₂, SrZn₂P₂, and CaZn₂P₂ as candidate materials based on the properties calculated, besides ZnCa₂N₂ and ZnSr₂N₂, which are susceptible to Vac_N formation.

For the pnictides whose structures were unavailable in the ICSD, we calculated the ground state configuration by considering possible structures using other binary and ternary pnictide unit cells that were available as templates. However, we did not consider the possibility

of cation arrangements forming superlattices over larger distances, which requires the consideration of larger supercells (instead of smaller unit cells), thus significantly increasing computational costs. Thus, for the candidate ternaries that we have identified (namely, SrZn_2N_2 , SrZn_2P_2 , and CaZn_2P_2), it may be useful to explore the possibility of superlattice formation. Also, we did not consider the anti-bixbyite structure of $\text{Ca}_3\text{N}_2/\text{Zn}_3\text{N}_2$ as templates for the ternary and quaternary structures since the structure has 48 symmetrically distinct cation sites and decorating, say, 16 sites each of Ca, Sr, and Zn is computationally intractable. Hence, we do not rule out our candidate ternaries from crystallizing in anti-bixbyite-based structures.

We carried out DOS calculations using SCAN and HSE06 because the former typically underestimates E_g . Since hybrid functionals include a portion of the exact exchange, their band gap estimates are typically better due to the consequent reduction in self-interaction errors compared to semi-local functionals. Indeed, previous studies have reported better agreement in band gap estimates with HSE06 vs. experiments compared to SCAN in kesterite photovoltaics.⁽⁵⁰⁾⁻⁽⁵³⁾ However, hybrid functionals do not guarantee the best theoretical estimates of E_g , which typically require quasi-particle calculations, such as the single-shot GW calculation (i.e., G_0W_0), which has shown excellent agreement with experimental photoemission spectroscopy/inverse photoemission spectroscopy measurements before.^(54,55) However, the computational costs of GW calculations are even higher than hybrid functionals, which is the reason we did not pursue such calculations for all the twenty compounds considered in our work.

The synthesis of nitrides is difficult given their tendency to decompose at higher temperatures due to lower formation energies (compared to oxides),⁽¹²⁾ the strong triple bond of N_2 molecule, and stringent conditions of oxygen and water-free conditions to achieve high purity.^(56,57) Hence, we have focused solely on compounds that are stable at 0 K since we expect the synthesis to be easier compared to metastable compounds ($E^{\text{hull}} \leq 30$ meV/atom), which may require higher temperatures and/or pressures. So far, synthesis of Ca and Zn based ternary nitrides have been performed via solid state techniques, using binary Ca_3N_2 and Zn_3N_2 as precursors,⁽¹²⁾ where ZnCa_2N_2 required Ar-atmosphere and CaZn_2N_2 needed high pressure and an elevated temperature.⁽¹²⁾ Besides synthesis difficulties, the air and moisture sensitivity of the candidate compounds (both nitrides and phosphides), particularly during operation as a photovoltaic, and the consequent impact on solar absorption efficiencies remains to be quantified. In the case of phosphides, the possible formation of the highly-toxic phosphine gas, either during synthesis or during operation, is also a concern.⁽⁵⁸⁾⁻⁽⁵⁹⁾ Another challenge with

pnictides will be the ability to form *p-n* homojunctions, instead of relying on other materials to form heterojunction-based devices.⁽⁴⁶⁾

While DFT often does not provide quantitative accuracy for defect formation energies, previous studies have shown that SCAN can provide an upper bound (compared to other semi-local functionals) on defect formation energies, with qualitative trends being similar across different functionals for a given compound.⁽³⁰⁾⁻⁽³⁶⁾ For reducing quantitative error in defect formation energies, we need further improvements in the XC functional and likely shoulder higher computational costs. Nevertheless, we expect all candidate pnictides shown in **Figure 4** to be significantly more resistant to point defect formation, such as cation vacancies, cation anti-sites, and anion vacancies, compared to other compound semiconductors, such as $\text{Cu}_2\text{ZnSnS}_4$.

5 Conclusion

The design of new semiconducting beyond-Si materials that can achieve reasonable solar-to-electricity conversion efficiencies, and that consist of relatively abundant and non-toxic elements is a key ingredient in moving towards non-fossil-fuel-based sources of energy. In this work, we have used DFT calculations to systematically explore the pnictide chemical space, including binary A_3B_2 , ternary $\text{AA}'_2\text{B}_2$, and quaternary $\text{AA}'\text{A}''\text{B}_2$ compounds, where A, A', and A'' are non-redox-active divalent cations (namely Ca, Sr, or Zn), and B is either N or P. In total, we considered a set of 20 pnictide compositions, out of which 10 were experimentally known structures and we created the initial (theoretical) structures of the remaining 10 compounds using experimentally-available template structures. Upon identifying the DFT-calculated ground state configurations of all 20 compositions, we evaluated the band gaps, 0 K thermodynamic and dynamic stability, and the resistance to formation of cation/anion vacancies and cation anti-sites. For treating the electronic exchange and correlation, we used a combination of the SCAN and HSE06 functionals, with SCAN used for structure relaxations and HSE06 for band gap evaluations. Wherever possible, we benchmarked our calculated values with those available in the literature. Importantly, we found a set of five pnictide compositions that exhibit HSE06-calculated band gaps in the optimal (1.1-1.5 eV) range, are thermodynamically stable at 0 K, and are resistant to formation of point defects (formation energy > 0.4 eV), namely, SrZn_2N_2 , SrZn_2P_2 , CaZn_2P_2 , ZnCa_2N_2 , and ZnSr_2N_2 . Among the

candidates identified, we found SrZn_2N_2 , SrZn_2P_2 , and CaZn_2P_2 to be particularly resistant to forming point defects (formation energies >1 eV), while the other compounds (ZnCa_2N_2 and ZnSr_2N_2) are susceptible to Vac_N formation (0.42-0.47 eV). We hope that our study will ignite further interest in the pnictide chemical space and enable the practical realization of some of the candidates identified in this work as beyond-Si photovoltaics.

Electronic Supporting Information

PAW potentials used, SCAN and HSE06 calculated DOS data, range of chemical potentials used for defect calculations, and structural information on all theoretical structures considered.

Data Availability

All the computational data presented in this study are freely available to all on our GitHub repository (<https://github.com/sai-mat-group/pv-nitrides>).

Acknowledgments

G.S.G acknowledges financial support from the Indian Institute of Science (IISc) Seed Grant, SG/MHRD/20/0020 and SR/MHRD/20/0013. J.K. thanks the Ministry of Human Resource Development, Government of India, for financial assistance. The authors acknowledge the computational resources provided by the Supercomputer Education and Research Centre, IISc, for enabling some of the density functional theory calculations showcased in this work.

References

View Article Online
DOI: 10.1039/D2CP04453F

1. www.futureforall.org/energy/solar_energy.htm
2. Shockley W, Queisser HJ. Detailed Balance Limit of Efficiency of p-n Junction Solar Cells. *J App Phys*. 2015;510.
3. Gautam GS, Senftle TP, Carter EA. Understanding the Effects of Cd and Ag Doping in Cu₂ZnSnS₄ Solar Cells. *Chem Mater*. 2018;30:4543-55
4. Lee TD, Ebong AU. A review of thin film solar cell technologies and challenges. *Renew Sustain Energy Rev*. 2017;70:1286–97.
5. Feurer T, Reinhard P, Avancini E, Bissig B, Löckinger J, Fuchs P, et al. Progress in thin film CIGS photovoltaics – Research and development, manufacturing, and applications. *Prog Photovoltaics Res Appl*. 2017;25(7):645–67.
6. Sharma S, Jain KK, Sharma A. Solar Cells: In Research and Applications—A Review. *Mater Sci Appl*. 2015;06(12):1145–55.
7. Editorial. Elements in short supply. *Nat Mater*. 2011;10(3):157.
8. Chen L, Soltanmohammad S, Lee JW, McCandless BE, Shafarman WN. Secondary phase formation in (Ag,Cu)(In,Ga)Se₂ thin films grown by three-stage co-evaporation. *Sol Energy Mater Sol Cells*. 2017;166:18–26.
9. Hohenberg P, Kohn W. Inhomogeneous electron gas. *Phys rev*. 1964;136:B864-71.
10. Kohn W, Sham LJ. Self-consistent equations including exchange and correlation effects. *Phys rev*. 1965;140:A1133-8.
11. Kikuchi R, Ueno K, Nakamura T, Kurabuchi T, Kaneko Y, Kumagai Y, et al. SrZn₂N₂ as a Solar Absorber: Theoretical Defect Chemistry and Synthesis by Metal Alloy Nitridation. *Chem Mater*. 2021;33(8):2864–70.
12. Hinuma Y, Hatakeyama T, Kumagai Y, Burton LA, Sato H, Muraba Y, et al. Discovery of earth-abundant nitride semiconductors by computational screening and high-pressure synthesis. *Nat Commun*. 2016; 1–2.
13. Tsuji M, Hiramatsu H, Hosono H. Tunable Light Emission through the Range 1.8-3.2 eV and p-Type Conductivity at Room Temperature for Nitride Semiconductors, Ca(Mg_(1-x)Zn_(x))₂N₂ (x = 0-1). *Inorg Chem*. 2019;58(18):12311–16.
14. Murtaza G, Khan AA, AL-Anazy MM, Laref A, Mahmood Q, Zada Z, et al. Anionic variations for BaMg₂X₂ (X = N to Bi) compounds by density functional theory. *Eur Phys J Plus* 2021;136(2):1–16.
15. Orhan E, Jobic S, Brec R, Marchand R, Saillard J. Binary nitrides α -M₃N₂ (M - Be,Mg,Ca): a theoretical study. *J Mater Chem* 2002;2:2475–9.
16. Pawlikowski JM, Misiewicz J, and Mirowska N. Direct and indirect optical transitions in Zn₃P₂. *J Phys Chem Solids* 1979;40:1027-1033.
17. Pawlikowski JM. Optical band gap of Cd₃P₂-Zn₃P₂ semiconductor solid solutions. *J Phys C*. 1985;18:5605-16.
18. Long R, Dai Y, Yu L, Huang B, Han S. Atomic geometry and electronic structure of defects in Zn₃N₂. *Thin Solid Films*. 2008;516:1297–301.

19. Greenaway AL, Melamed CL, Tellekamp MB, Woods-Robinson R, Toberer ES, Neilson JR, et al. Ternary Nitride Materials: Fundamentals and Emerging Device Applications. *Annu Rev Mater Res*. 2021;51:591–618. View Article Online
DOI: 10.1039/D2CP04453F
20. Sun W, Bartel CJ, Arca E, Bauers SR, Matthews B, Orvañanos B, et al. A map of the inorganic ternary metal nitrides. *Nat Mater*. 2019;18(7):732–9.
21. Kresse G, Hafner J. Ab initio molecular dynamics for liquid metals. *Phys Rev B*. 1993;47(1):558–61.
22. Kresse G, Furthmu J. Efficient iterative schemes for ab initio total-energy calculations using a plane-wave basis set. *Phys Rev B*. 1996;54(16).
23. Kresse G, Joubert D. From ultrasoft pseudopotentials to the projector augmented-wave method. *Phys Rev B*. 1999;59(3):11–9.
24. Monkhorst HJ & Pack JD, Special points for Brillouin-zone integrations. *Phys rev B*. 1976;13:5188–92.
25. Sun J, Ruzsinszky A, Perdew JP. Strongly Constrained and Appropriately Normed Semilocal Density Functional. *Phys Rev Lett*. 2015;036402:1–6.
26. Sai Gautam G, Carter EA. Evaluating transition metal oxides within DFT-SCAN and SCAN+U frameworks for solar thermochemical applications. *Phys Rev Mater*. 2018;2(9):1–14.
27. Long OY, Sai Gautam G, Carter EA. Evaluating optimal U for 3d transition-metal oxides within the SCAN+ U framework. *Phys Rev Mater*. 2020;4(4):1–15.
28. Long OY, Sai Gautam G, Carter EA. Assessing cathode property prediction: Via exchange-correlation functionals with and without long-range dispersion corrections. *Phys Chem Chem Phys*. 2021;23(43):24726–37.
29. Berman S, Sai Gautam G, Carter EA. Role of Na and Ca as Isovalent Dopants in Cu₂ZnSnS₄ Solar Cells. *ACS Sustain Chem Eng*. 2019;7(6):5792–800.
30. Wexler RB, Gautam GS, Carter EA. Exchange-correlation functional challenges in modeling quaternary chalcogenides. *Phys Rev B*. 2020;102(5):54101.
31. Heyd J, Scuseria GE, Ernzerhof M. Hybrid functionals based on a screened Coulomb potential. *J Chem Phys*. 2003;118(18):8207–15.
32. Setyawan W, Curtarolo S. High-throughput electronic band structure calculations: Challenges and tools. *Comput Mater Sci*. 2010;49(2):299–312.
33. Ping S, Davidson W, Jain A, Hautier G, Kocher M, Cholia S, et al. Python Materials Genomics (pymatgen): A robust, open-source python library for materials analysis. *Comput Mater Sci*. 2013;68:314–19.
34. Hellenbrandt M. The inorganic crystal structure database (ICSD) - Present and future. *Crystallogr Rev*. 2004;10(1):17–22.
35. Togo A, Tanaka I. First principles phonon calculations in materials science. *Scr Mater*. 2015;108:1–5.
36. Freysoldt C, Grabowski B, Hickel T, Neugebauer J, Kresse G, Janotti A, et al. First-principles calculations for point defects in solids. *Rev Mod Phys*. 2014;86:253–305.

37. Heyns AM, Prinsloo LC, Stassen M. The Vibrational Spectra and Decomposition of Calcium Nitride (Ca_3N_2) and Magnesium Nitride (Mg_3N_2) J Solid State Chem. 1998;41(137):33–41.
38. Zanin IE, Aleinikova KB, Afanasiev MM, Antipin MY. Structure of Zn_3P_2 . J Structural Chem. 2004;45(5):844–8.
39. Yamane H, Disalvo FJ. Synthesis and Crystal Structure of Sr_2ZnN_2 and Ba_2ZnN_2 . J Solid State Chem. 1995;379:375–9.
40. Klufers P, Mewis A. AB_2X_2 Compounds with the CaAl_2Si_2 Structure, II1 ($\text{A} = \text{Ca}$; $\text{B} = \text{Zn}$, Cd ; $\text{X} = \text{P}$, As) Z Naturforsch. 1977;32:353–4
41. Xie LS, Schoop LM, Seibel EM. A new form of Ca_3P_2 with a ring of Dirac nodes. APL Mater. 2015;3:083602.
42. Wilson DK, Saparov B, Bobev S. Synthesis , Crystal Structures and Properties of the Zintl Phases Sr_2ZnP_2 , Sr_2ZnAs_2 , A_2ZnSb_2 and A_2ZnBi_2 ($\text{A} = \text{Sr}$ and Eu). J Inorg Gen Chem. 2018;2:2018–25.
43. Zong F, Ma H, Xue C, Zhuang H, Zhang X. Synthesis and thermal stability of Zn_3N_2 powder. Solid State Comm. 2004;132:521–5.
44. Tran F, Blaha P. Accurate band gaps of semiconductors and insulators with a semilocal exchange-correlation potential. Phys Rev Lett. 2009;102(22):5–8.
45. Balci GK, Ayhan S. S. The first principle study: Structural, electronic and optical properties of X_2ZnN_2 ($\text{X} : \text{Ca}$, Ba , Sr). J Non-Oxide Glasses. 2019;11(1):9–18.
46. Kimball GM, Lewis NS, Atwater HA. Mg doping and alloying in Zn_3P_2 heterojunction solar cells. Conf Rec IEEE Photovolt Spec Conf. 2010;1039–43.
47. Suda T, Kakishita K. Band-gap energy and electron effective mass of polycrystalline Zn_3N_2 . J Appl Phys. 2006;99(7):1–4.
48. Wu P, Cao X, Tiedje T, Yamada N. Bandgap tunable $\text{Zn}_{3-3x}\text{Mg}_{3x}\text{N}_2$ alloy for earth-abundant solar absorber. Mater Lett. 2019;236:649–52.
49. Lu W, Wang J, Sai Gautam G, Canepa P. Searching Ternary Oxides and Chalcogenides as Positive Electrodes for Calcium Batteries. Chem Mater. 2021;33(14):5809–21.
50. Gautam GS, Wexler RB, Carter EA. Optimizing kesterite solar cells from $\text{Cu}_2\text{ZnSnS}_4$ to $\text{Cu}_2\text{CdGe}(\text{S},\text{Se})_4$. J Mater Chem. 2021;39:9882–97.
51. Hadke S, Levchenko S, Sai Gautam G, Hages CJ, Márquez JA, Izquierdo-Roca V, et al. Suppressed Deep Traps and Bandgap Fluctuations in $\text{Cu}_2\text{CdSnS}_4$ Solar Cells with $\approx 8\%$ Efficiency. Adv Energy Mater. 2019;9(45):1–11.
52. Chen S, Yang J, Gong XG. Intrinsic point defects and complexes in the quaternary kesterite semiconductor $\text{Cu}_2\text{ZnSnS}_4$. Phys Rev B. 2010;35–7.
53. Chen S, Walsh A, Gong XG, Wei SH. Classification of lattice defects in the kesterite $\text{Cu}_2\text{ZnSnS}_4$ and $\text{Cu}_2\text{ZnSnSe}_4$ earth-abundant solar cell absorbers. Adv Mater. 2013;25(11):1522–39.
54. Alidoust N, Lessio M, Carter EA. Cobalt (II) oxide and nickel (II) oxide alloys as potential intermediate-band semiconductors: A theoretical study. J Appl Phys.

2016;119(2).

View Article Online
DOI: 10.1039/D2CP04453F

55. Alidoust N, Toroker MC, Keith JA, Carter EA. Significant reduction in NiO band gap upon formation of $\text{Li}_x\text{Ni}_{1-x}\text{O}$ alloys: Applications to solar energy conversion. *Chem Sus Chem*. 2014;7(1):195–201.
56. Elder SH, DiSalvo FJ. Thermodynamics of Ternary Nitride Formation by Ammonolysis: Application to LiMoN_2 , Na_3WN_3 , and $\text{Na}_3\text{WO}_3\text{N}$. *Chem Mater*. 1993;(22):1545–53.
57. McHale JM, Navrotsky A, Kowach GR, Balbarin VE, Disalvo FJ. Energetics of Ternary Nitrides: Li-Ca-Zn-N and Ca-Ta-N Systems. *Chem Mater*. 1997;9(7):1538–46.
58. Rothfelder R, Streitferdt V, Lennert U, Cammarata J, Scott DJ, Zeitler K, et al. Photocatalytic Arylation of P4 and PH3: Reaction Development Through Mechanistic Insight. *Angew Chemie - Int Ed*. 2021;60(46):24650–8.
59. Kakishita K, Ikeda S, Suda T. Zn_3P_2 epitaxial growth by MOCVD. *J Cryst Growth*. 1991;115(1–4):793–7.